Nanoscale

PAPER

View Article Online
View Journal | View Issue

Cite this: *Nanoscale*, 2019, **11**, 9626

Enhanced-performance of self-powered flexible quantum dot photodetectors by a double hole transport layer structure†

Ting Shen,[a] David Binks,[b] Jifeng Yuan,[a] Guozhong Cao [c] and Jianjun Tian *[a]

Received 2nd February 2019,
Accepted 28th April 2019

DOI: 10.1039/c9nr01096c

rsc.li/nanoscale

The usefulness of self-powered quantum dot (QD) photodetectors is increased if they are fabricated on flexible substrates. However, the performance of such photodetectors is typically significantly worse than similar devices fabricated on glass substrates due to poor charge transport performance. Here, a novel flexible self-powered $CdSe_xTe_{1-x}$ QD photodetector with a double hole transport layer of PEDOT:PSS/P-TPD has been fabricated, which achieves a performance comparable to that of rigid devices. The energy level of the P-TPD layer matches well with that of the PEDOT:PSS and QD layers, which significantly enhances photodetection capability across a spectral region that spans the ultraviolet, visible and near infrared (UV-NIR). A low dark current density (1.03×10^{-6} mA cm^{-2}) and a large specific detectivity of approximately 2.6×10^{12} Jones at a wavelength of 450 nm are demonstrated, significantly outperforming previously reported flexible QD-based detectors. This improvement in performance is attributed to both increased hole transport efficiency and the inhibition of electron transport from the QDs into the PEDOT:PSS layer. The photodetector also exhibits good sensitivity under weak illumination, producing a photocurrent of 196×10^{-6} mA cm^{-2} under an irradiance of 5 μW cm^{-2}. Moreover, no significant performance degradation is observed after 150 bending cycles to an angle of 60 degrees.

1. Introduction

Quantum dots (QDs) have drawn great attention due to their promising electronic and optoelectronic characteristics,[1] for instance, widely tunable bandgap,[2] large light absorption coefficient,[3,4] and high photochemical stability.[5] Furthermore, QDs can be easily synthesised and processed by solution-based methods.[6] These significant properties have led to broad application, such as in solar cells,[7–9] light-emitting diodes,[10] lasers[11] and photodetectors.[12] Specifically, photodetectors are widely applied in chemical sensing, light imaging, optical communications, industrial manufacturing, environmental monitoring and medical analysis.[13–15] The quantum confinement effect in QDs increases the bandgap with reducing size,[16] leading to low thermal excitation, and hence lower dark currents and higher operating temperatures. Therefore, QDs are recognized as promising materials for demanding photodetector applications.[17–19] Self-powered (*i.e.* photovoltaic) photodetectors typically have lower dark currents and faster response speeds than Schottky type devices,[20] allowing them to operate at higher frequency with lower noise.

Furthermore, to realize intelligent electronic systems, there is an increasing demand to combine optoelectronic functionality with other characteristics that make a device more suited to applications[21,22] such as shock resistance, portability and flexibility.[19,23,24] For instance, flexible devices can be attached to curved surfaces or skin or woven into garments to realize detection or optical communication.[23,25] Thus, a flexible self-powered photodetector with broadband response, fast speed, high detectivity, excellent weak-light responsivity and stability would be well suited to many applications. However, the performance of flexible photodetectors is currently significantly worse than that of similar devices fabricated on glass substrates. In particular, the detectivity of flexible photodetectors is 10 times less than that of rigid devices with the same photosensitive materials and architecture.[22,26] Therefore, new designs are required for flexible photodetectors so that they can match the performance of rigid devices.

Bearing this in mind, a novel photodetector with a bulk-heterojunction architecture comprising PEDOT:PSS/poly (*N*,*N*9-bis (4-butylphenyl)-*N*,*N*9-bis(phenyl)-benzidine) (P-TPD)/QDs/ZnO

[a]*Institute for Advanced Materials and Technology, University of Science and Technology Beijing, Beijing, 100083, China. E-mail: tianjianjun@mater.ustb.edu.cn*
[b]*School of Physics and Astronomy and Photon Science Institute, University of Manchester, Manchester, M13 9PL, UK*
[c]*Department of Materials and Engineering, University of Washington, Seattle, WA, 98195-2120, USA*

†Electronic supplementary information (ESI) available. See DOI: 10.1039/c9nr01096c

fabricated onto a flexible polyethylene terephthalate substrate is first demonstrated in this work. The double hole transport layer (HTL) of PEDOT:PSS and P-TPD used results in improved hole transport and enhances the detector response to UV-NIR light. Furthermore, P-TPD has a high-lying lowest unoccupied molecular orbital (LUMO) level which enables it to act as an effective electron blocking layer, suppressing electron–hole recombination. Thus, enhanced UV-NIR photodetection capability was obtained, with a detectivity (D^*) of 2.6×10^{12} Jones, a detector responsivity (R) of 45 mA W^{-1}, a high on–off ratio (I_{on}/I_{off}) of 9.9×10^5 under a power of 100 mW cm^{-2}, and a short rise/decay time (t_r/t_d = 40 ms). In addition, the double HTL-based photodetector displayed a high photocurrent response (196×10^{-6} mA cm^{-2}) even under weak illumination (5 μW cm^{-2}), making it well-suited for low light detection. Moreover, the flexible device demonstrated negligible degradation in performance after 150 bending cycles. Thus, a self-powered, flexible QD-based photodetector, with high specific detectivity, responsivity, durability and stability, has been demonstrated providing a promising route for monitoring, diagnosis and imaging applications.

2. Experimental

Synthesis method

Preparation of Cd, Se, and Te precursors: 0.411 g of CdO powder (0.0316 g of Se powder, 1 ml TOP and 3 ml paraffin liquid/0.038 g of Te powder, and 0.75 ml TOP and 2.25 ml paraffin liquid) were loaded into a 50 ml 3-necked flask containing 24 ml of paraffin liquid and 8 ml of oleic acid, degassed for 40 min before 90 °C, and subsequently heated up to 260 °C under a nitrogen atmosphere until all powders were dissolved and the solution became clear (for Se and Te precursors, the reaction temperature was 150 °C and 300 °C, respectively). The three precursor solutions were stored in N_2 at 50 °C until they were needed for the QD synthesis.

The reaction mixture with a Cd : Se : Te molar ratio of 10 : 1 : 1 was stirred in a 100 ml-three-necked flask and degassed for 40 min at 90 °C. The flask was purged with N_2 and then placed back under vacuum. This process of alternately applying vacuum and N_2 was repeated for a total of 3 times to remove H_2O and O_2. The flask was always under vacuum until no gas was released from the solution and then heated up to 310 °C at a rate of 30 °C min^{-1} under a nitrogen atmosphere along with vigorous stirring. After reacting for 3 min, the reaction mixture was cooled to 260 °C, and 2 ml of oleylamine was swiftly injected into the solution to limit the growth of the nanocrystals. The solution was then allowed to cool to 60 °C by removing the heater. $CdSe_xTe_{1-x}$ QDs with a diameter of 5.1 ± 0.2 nm, were obtained after cleaning and purification.

Device fabrication

The PEDOT:PSS solution was spin-coated at 4000 rpm onto a cleaned ITO/PET substrate for 60 s and then heated up to 110 °C, before transferring into a nitrogen-filled glove box after 20 min. P-TPD, $CdSe_xTe_{1-x}$ QDs and ZnO solutions were spin-coated layer-by-layer at 2500 rpm for 30 s. The P-TPD layer was heated at 110 °C for 20 min before the deposition of the next layer. The QD layer and the ZnO layer were baked at 80 °C for 20 min. Al electrodes were deposited using a thermal evaporation system under a vacuum of $\sim -10^{-4}$ torr.

Device characterization

The absorption spectra of the colloidal $Cd_xSe_{1-x}Te$ QDs were recorded using a UV-visible spectrophotometer (T10CS) over a wavelength range of 300 nm to 900 nm. XRD measurements were performed with an X-ray diffractometer (PANalytical EPSILON5) using monochromatic Cu Kα radiation and a voltage of 30 kV and a current of 30 mA. The PL spectrum was acquired using a photoluminescence spectrometer (FL-380, Gangdong Sci. & Tech. Development Co., LTD, Tianjin, China) from 350 nm to 850 nm, for an excitation wavelength of 470 nm. The responsivity spectra were obtained in a direct current mode over the range 300–850 nm. The measurement system is composed of a Keithley 2400 multimeter as a digital source meter, a 150 W xenon lamp and a 7 Star Optical Instruments 7ISW30 monochromator. An electrochemical workstation (CH Instruments, Inc., Shanghai, China) was employed for electrochemical impedance spectroscopy (EIS) and the photocurrent response under light switching was obtained using a 71S0503A solar simulator (7 star Optical Instruments Co., Beijing, China) with an output intensity of ~100 mW cm^{-2}. 3A grade AM 1.5 simulated sunlight with an output power of ~100 mW cm^{-2} was used to obtain the I–V characteristics of the devices. The SEM images were taken using a Hitachi SU8020 scanning electron microscope which incorporates an energy-dispersive X-ray (EDX) spectrometer. A Phoenix 600 Contact Angle Meter was employed to measure the contact angles. The TEM images were taken with a JEM-2010 transmission electron microscope.

The detectivity (D^*) is calculated using the equation:[12,27,28]

$$D^* = R\frac{1}{\sqrt{2qI_{dark}/S}}$$

where R is the responsivity, I_{dark} is the dark current, S is the active area of the device, the active area is 0.1007 cm^2, and q is the elementary charge. For a self-powered detector, the shot noise from the dark current is the major contribution to the noise current, and arises from the change of the diffusion rate caused by random thermal movement and the random fluctuations of the carrier density caused by thermal generation-recombination. Thus the noise current can be directly inferred from the dark current in self-powered detectors.

3. Results and discussion

The device structure of the flexible self-powered QD-based photodetector with single HTL and double HTL is displayed schematically in Fig. 1a and b, respectively. Here, p-type poly(*N*,*N*9-bis(4-butylphenyl)-*N*,*N*9-bis(phenyl)-benzidine) (P-TPD)

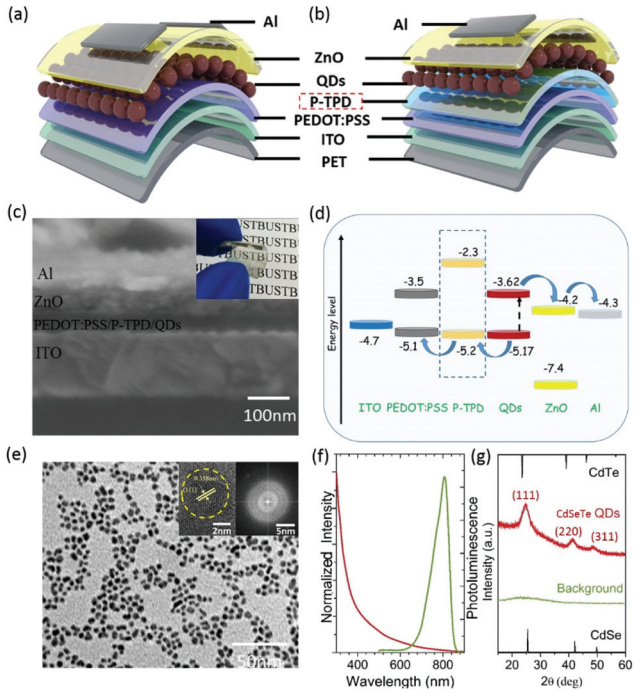

Fig. 1 Schematic diagram of the devices with single HTL layer (a) and double HTL layer (b), respectively. (c) Cross-sectional SEM image with an image of the device inset, and (d) energy band diagram of the photodetector with double HTL layer. (e) TEM image, with inset images of HRTEM and SAED, (f) absorption (red line) and steady-state photoluminescence (PL) spectra (green line, λ_{ex} = 470 nm) and (g) X-ray diffraction (XRD) pattern of the $CdSe_xTe_{1-x}$ QDs.

was spin coated onto a PEDOT:PSS layer to form the double HTL. A cross-sectional scanning electron microscopy (SEM) image of the device with double HTL is shown in Fig. 1c, which is stacked in the structural sequence of the Al electrode/ZnO electron transport layer (ETL)/$CdSe_xTe_{1-x}$ QD layer/P-TPD/PEDOT:PSS/tin-oxide doped with indium/polyethylene terephthalate (ITO/PET). The transparency and flexibility of the device can be observed from the inset image in Fig. 1c. The energy level diagram for the photodetector in Fig. 1d indicates that electrons are injected into the ZnO ETL, and holes are transported *via* the P-TPD and PEDOT:PSS double HTL. As can be seen from the energy band diagram, the energy gap between the highest occupied molecular orbital (HOMO) level of the P-TPD and the valence band maximum (VBM) of the $CdSe_xTe_{1-x}$ QDs is only 0.03 eV and so facilitates hole injection. Moreover, the 1.3 eV difference between the P-TPD LUMO level and the conduction band minimum (CBM) of the $CdSe_xTe_{1-x}$ QDs makes P-TPD an effective electron blocking material, inhibiting charge recombination and thereby improving device performance. However, the experimental results below indicate that the device with only one layer of P-TPD as the HTL has comparatively poor performance, likely due to the large difference between the VBM of ITO and the LUMO level of P-TPD.

Transmission electron microscopy (TEM) of the colloidal $CdSe_xTe_{1-x}$ QDs, see Fig. 1e, was used to determine their size and shape and shows them to be of nearly spherical shape with a narrow size distribution (without any post-preparation fractionation or size sorting) and have an average particle size of 5.1 ± 0.2 nm. (The composition of $CdSe_xTe_{1-x}$ is close to $CdSe_{0.67}Te_{0.33}$, which is confirmed by EDX as shown in Fig. S1.†) The inset in Fig. 1e shows a high resolution TEM (HRTEM) image of a QD, in which the lattice fringes for $CdSe_xTe_{1-x}$ are clearly evident in the selected area electron diffraction (SAED) pattern, indicating good crystallinity. The lattice spacing of 0.358 nm, as shown in the HRTEM image, is in good agreement with the values for the (111) plane for both zinc blende CdSe (JCPDS card no. 19-0191, lattice spacing: 0.351 nm) and CdTe (JCPDS card no. 65-1081, lattice spacing: 0.374 nm). Fig. 1f shows the absorption and steady-state photoluminescence (PL) spectra for the $CdSe_xTe_{1-x}$ QDs. The onset of absorption is at about 800 nm while the PL peak is centred at 810 nm, demonstrating the NIR band edge of the QDs. It thus possesses a light harvesting range well-matched to the solar spectrum and the emission of artificial lighting. The X-ray diffraction (XRD) pattern shown in Fig. 1g confirms the presence of $CdSe_xTe_{1-x}$ QDs. The sample exhibits well-resolved diffraction peaks characteristic of $CdSe_xTe_{1-x}$. In particular, it has strong peaks at 24.7° and 41.4°, which lie between the standard values for zinc blende CdSe (JCPDS card no. 19-0191) and CdTe (JCPDS card no. 65-1081). It is thus consistent with the TEM analysis. The wide diffraction peaks are attributed to the small size of the QDs.[16,29]

Fig. 2a compares the current–voltage (*I–V*) response for devices fabricated with single HTL and double HTL (the performance of the two devices without the QD-photodetector incorporating a double PEDOT:PSS/P-TPD HTL structure was determined *via* solution-processing methods onto a flexible substrate). By the addition of P-TPD to form a double HTL, the

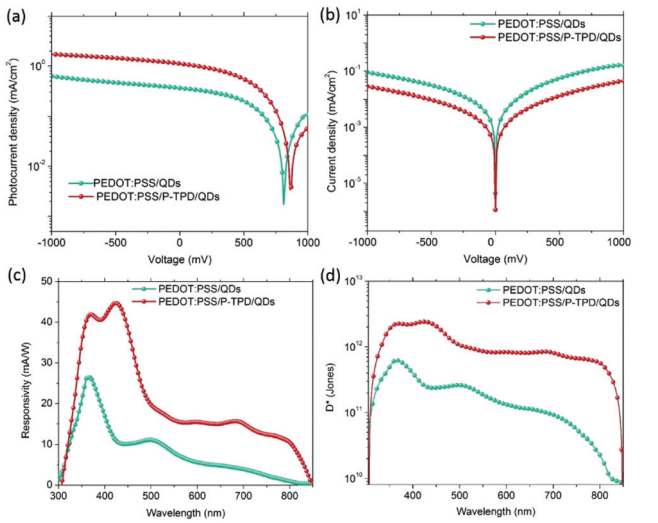

Fig. 2 Current–voltage characteristic under a white light illumination of 100 mW cm^{-2} (a) and in the dark (b). Responsivity (c) and detectivity (d) of the single HTL and double HTL devices under a bias of 0 V as a function of wavelength (from 300 nm to 850 nm).

hole transport efficiency was significantly enhanced. Due to the high LUMO energy level of the P-TPD, electron transport to the HTL was effectively blocked. As a consequence, the photodetector exhibited a broad spectral response encompassing the ultraviolet-visible-near infrared (UV-NIR) region, a high specific detectivity of 2.6×10^{12} Jones, a fast response speed of 40 ms, and a high responsivity of 45 mA W^{-1} with extreme flexibility. The detectivity is higher that of the reported flexible QD-photodetectors, and is comparable to rigid devices with the same architecture. More importantly, an excellent photocurrent density (196×10^{-6} mA cm^{-2}) was observed for the double HTL-based photodetector under weak light illumination (5 μW cm^{-2}). The flexible device also showed excellent folding endurance and electrical stability after bending 150 cycles. Our results suggest that such high-performance flexible photodetectors may have great potential for monitoring, communications and imaging applications. $CdSe_xTe_{1-x}$ QDs were also tested; more details can be found in Fig. S2 of the ESI†), from which excellent rectifying behaviors can be observed for both the devices. The double HTL-based detector shows a significantly higher photocurrent density (1.12 mA cm^{-2}) than the single HTL-based devices (0.37 mA cm^{-2}). A rectification ratio as high as 9.9×10^5 was found for the double HTL-based device, and its open-circuit voltage was calculated to be 0.78 V. (The optimization of the devices are shown in Fig. S3 and S4.†) This can be ascribed to the fast hole transport and effective suppression of charge recombination. The mobility of holes in P-TPD (1.0×10^{-4} cm^2 V^{-1} s^{-1}) is more than two times higher than that of PEDOT:PSS (4.0×10^{-5} cm^2 V^{-1} s^{-1}).[30] In addition, the large band offset of 1.3 eV (see Fig. 1b) constitutes an effective barrier to electron transport from the QDs to PEDOT:PSS, reducing charge recombination. Such a reduction in recombination can lead to a high photocurrent and low dark current density.[31] The lower dark current density for the device with double HTL, as shown in Fig. 2b, demonstrates that this design can significantly decrease the leakage of current. The lower dark current will also result in a faster response speed and high detectivity.[32,33] Responsivity (R) is a measure of the current output per optical input and is a key factor that determines the device sensitivity.[34,35] From Fig. 2c, the responsivities of the double HTL-based device for excitation at wavelengths of 350 nm, 450 nm and 800 nm at a power of 100 mW cm^{-2} are 37.0, 41.5 and 10.5 mA W^{-1}, respectively, which are 1.8, 4.0 and 3.5 times larger than those of the single HTL-based device. In addition, the photoresponsivity spectra correspond to the absorption spectra of the $CdSe_xTe_{1-x}$ QDs shown in Fig. 1f. The detectivity (D^*)[36–41] characterises the ability of photodetectors to detect light, and the D^* spectra for the single and double devices are compared in Fig. 2d. It is worth noting that the double HTL-based photodetector exhibits larger D^* than that of the single HTL-based photodetector across the entire wavelength range of 300–850 nm. The D^* of the double HTL-based device is up to 2.1×10^{12} Jones at 350 nm, 2.6×10^{12} Jones at 450 nm and 0.5×10^{12} Jones at 800 nm. These values are larger than those of previously reported flexible QD photodetectors, as summarized in Table S1.† Furthermore, rigid photodetectors with the same structure were prepared for comparison with the flexible devices. The properties of the devices based on the rigid and flexible substrates are listed in Table S2,† and demonstrate that flexible photodetectors can have comparable performance to those based on rigid substrates. This enhanced performance for a flexible device is attributed to the introduction of double HTL, which greatly enhances the charge collection efficiency of the device.

Reliability and response speed are often crucial parameters for photodetectors.[42–44] The on–off switching properties of both devices are shown in Fig. 3a (under 3A grade illumination power of 100 mW cm^{-2}). It is seen that the photocurrent remains nearly constant after six cycles of light switching, showing that both devices can be switched on and off repeatedly. The photocurrent rapidly reaches saturation under this illumination, and then drops quickly with the light off. This indicates that the device allows facile charge tunnelling and transportation. It is worth noting that the photocurrent density decreases with increasing time. A possible reason for this observation is that the carriers are rapidly generated by the light excitation to produce high current. These carriers are then gradually trapped, resulting in a reduction in the current until the traps are completely filled. Fig. 3b shows the more detailed transient photocurrent of the device, where one on–off cycle is shown. The rise and decay times, t_r, and t_d, respectively, for the double HTL-based device are both 40 ms, which is half the value obtained for the single HTL-based device (*i.e.* 80 ms). The greater response speed of the double HTL-based device could be associated with faster carrier separation, a greater hole transport rate and a decrease in charge recombi-

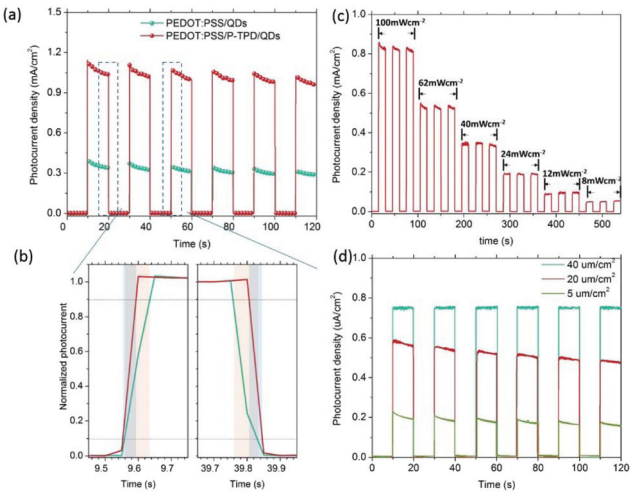

Fig. 3 (a) Current response of the devices under white light switching at 100 mW cm^{-2}. (The blue dashed line refers to the selected location of the magnified area below in (b).) (b) Single normalized switching characteristics of two devices to estimate response time at zero bias under white light illumination (at 100 mW cm^{-2}). (c) The photocurrent density of the device with double HTL under different optical powers. (d) The photocurrent density of the device under weak light at zero bias. The incident white light ranged in power from 40 μW cm^{-2} to 5 μW cm^{-2}.

nation in the device. The temporal evolution of V_{oc} for both detectors is shown in Fig. S5.† The double HTL-based photodetector possesses a higher voltage output and a faster voltage response speed than that of the single HTL-based photodetector. Light intensity-dependent measurements of photocurrent were employed to explore the response of the photodetector. Fig. 3c shows the photocurrent of the double HTL-based photodetector at different light intensities. The photocurrent of the devices is about 0.056 mA cm^{-2} at a low light intensity (8 mW cm^{-2}). We can observe good linear response of the device to light intensity for a decrease from 100 mW cm^{-2} to 8 mW cm^{-2}. The current levels remain nearly constant for three cycles at different light intensities. The 3 dB bandwidth of a photodetector is an important parameter to typically determine the temporal response. Both the carrier lifetime and the resistance–capacitance time of the circuit can determine the 3 dB bandwidth of the photodetector,[21] which is 200 Hz for the photodetector with double HTL as shown in Fig. S6,† indicating good frequency response. To explore the capability of the device for weak light detection, the photocurrent densities of the devices (under light switching) were detected under weak irradiances, as shown in Fig. 3d. We found that the generated photocurrent density was about 196 × 10^{-6} mA cm^{-2} for a light power of 5 μW cm^{-2}, which was hundred-fold higher than the dark current. Note that the photodetector with single HTL does not show such high sensitivity and requires a minimum light strength of 100 μW cm^{-2} for detection as shown in Fig. S7.† The double HTL device also performs well in the weak-light response compared to the previously reported photodetectors, as summarized in Table S3.† The response of the device to weak illumination is likely made possible for two main reasons. On the one hand, the P-TPD layer could be enhancing photodetection in the visible part of the spectrum (the absorbance curves of films with PEDOT:PSS and PEDOT:PSS/P-TPD are compared in Fig. S8 of the ESI†). On the other hand, P-TPD can facilitate the separation of the carriers, improve hole transport and enhance charge collection. This device thus has great potential in the field of weak light detection. It should be noted that the photodetector has good reproducibility with small standard deviation as shown in Fig. S9.† The average value of twelve devices for R is 40.10 ± 5.95 mA W^{-1} and for D^* is (2.30 ± 0.35) × 10^{12} Jones. The enhanced R and D^*, the higher on/off ratio, the outstanding response under the weak light and the fast light response for the double HTL-based device in comparison with those of the single HTL-based device all originated from the decreased charge recombination, increased photon harvesting and fast charge transfer.

To determine the transport properties, the I–V curves for hole-only versions of the devices were measured under dark conditions, as shown in Fig. 4a. The hole-only devices are composed of ITO/PEDOT:PSS/QDs/Al, ITO/P-TPD/QDs/Al and ITO/PEDOT:PSS/P-TPD/QDs/Al, respectively. Improved hole transport is demonstrated by higher current in the hole-only devices, which is determined by the product of the mobility, the steady-state charge density and the carrier lifetime in a

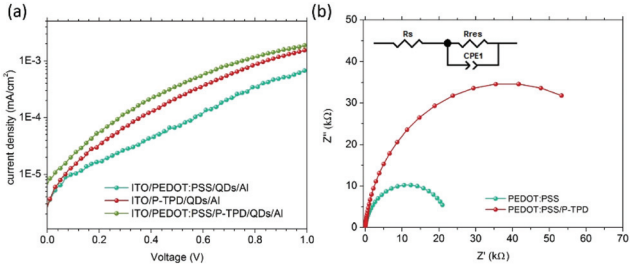

Fig. 4 (a) The dependence of dark current density on bias voltage for hole-only versions of the three devices (ITO/PEDOT:PSS/QDs/Al, ITO/P-TPD/QDs/Al and ITO/PEDOT:PSS/P-TPD/QDs/Al). (b) The electrochemical impedance spectroscopy (EIS) spectra of the devices with the PEDOT:PSS and PEDOT:PSS/P-TPD layer under dark conditions at a bias voltage equivalent to the open voltage of the devices. Inset: Equivalent circuit.

film.[41,45] The current densities of both ITO/P-TPD/QDs/Al and ITO/PEDOT:PSS/P-TPD/QDs/Al are significantly larger than that of ITO/PEDOT:PSS/QDs/Al. This suggests that the P-TPD can effectively facilitate hole transport into PEDOT:PSS and boost carrier collection. To explore the charge blocking capacity of the P-TPD layer on charge recombination, electrochemical impedance spectroscopy (EIS) was carried out. Fig. 4b displays the Nyquist plot of two devices at an applied bias equal to the open circuit voltage under dark conditions. In Fig. 4b, each semicircle characterizes the charge transport at the interface of the device, and can be represented by an equivalent circuit (inset of Fig. 4b) that consists of R_{rec}/CPE and R_s. Here, R_{rec} and CPE represent the impedance related to the charge transfer process and the interface capacitance, respectively. R_s indicates the series resistance of the entire device, which includes contributions from the conductive glass, wires and the interface of the device.[45,46] The double HTL-based device has a R_{rec} of 76.3 kΩ, whereas the single HTL-based device has a smaller value of 12.1 kΩ. R_{rec} reflects the ability to block charge recombination, which has an inversely-proportional relationship with the recombination rate.[47–49] The increase of R_{rec} thus indicates that there is a higher charge collection efficiency for devices with a double HTL. The P-TPD layer will inhibit recombination both by enhancing the separation and drift velocity of the electrons and holes, and by forming an effective energy barrier with its high HOMO level (−2.6 eV), preventing backflow of electrons. Moreover, the effect of the P-TPD layer on the solution wettability was investigated by contact angle measurements. The contact angles measured for an octane solution of QDs on the surface of PEDOT:PSS and PEDOT:PSS/P-TPD are 11.8° and 9.9°, respectively, as shown in Fig. S10.† The results indicate that the wettability of the QD solution is similar on both surfaces, and thus that the thickness of the QD film has not been significantly affected by the P-TPD layer.[50,51] Therefore, the enhanced photodetection capability of the double HTL-based photodetector is attributed to efficient hole transport in the P-TPD layer, and the inhibition of electron transport from the QDs

into the PEDOT:PSS layer, rather than a change in the thickness of the active layer ($CdSe_xTe_{1-x}$ QD film).

To further consider the stability of these devices as flexible photodetectors in practical applications, the effect of device folding on the electrical performance was investigated. Fig. 5a presents the steady-state photocurrent of the flexible devices with double HTL at various bending curvatures under a light intensity of 100 mW cm^{-2}. The optical images of the devices subjected to various bending angles are displayed in the insets of Fig. 5a. In this study, four different bending states were studied: I (0 degree), II (20 degrees), III (40 degrees) and IV (60 degrees). It can be seen that no obvious degradation in performance is detected in any of the four states for a photocurrent density of 0.98 mA cm^{-2} over 250 s, demonstrating the outstanding photocurrent stability of the device, which is unaffected by external bending stress. The photocurrent response of the devices under light periodically switched on and off was also tested for the four bending states as shown in Fig. 5b. The photocurrent of the flexible photodetector also remains nearly constant in these four bending states. It exhibits a similar response time even after the IV bending state as shown in Fig. S11.† In order to assess folding endurance, the electrical performance of the photodetector was measured after bending the devices through multiple cycles. The plots in Fig. 5c are the *I–V* characteristics of the photodetector after bending through as many as 150 cycles. It should be noted that the photocurrent still remains of the same order after folding the device through 150 cycles. After more than 300 cycles, it shows a decreasing trend for the photocurrent and photovoltage for the devices. And the decrease becomes obvious after 500 cycles. In addition, SEM images were used to evaluate any morphological changes of the films after different numbers of folding cycles. As shown in Fig. 5e and f, there are no microcracks or fissures evident in the films after folding for 50 or 150 cycles, and after folding a morphology is observed that is similar to the film before folding (Fig. 5d). The atomic force microscopy (AFM) images and corresponding surface roughness of the films are shown in Fig. S12.† After bending 500 cycles, the surface roughness increased corresponds to the decrease of photocurrent for the devices. These results demonstrate that the flexible double HTL-based QD photodetectors have good mechanical and electrical stability.

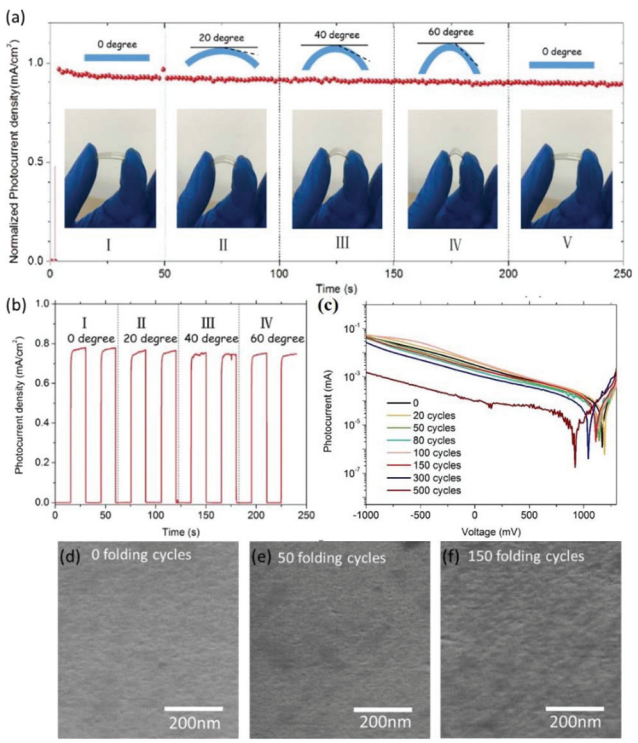

Fig. 5 Photocurrent response of the double HTL device (a) under constant illumination and (b) under switched light. (c) *I–V* characteristics of the flexible device after folding 0, 20, 50, 80, 100, 150, 300 and 500 cycles. Measurements were made under a light intensity of 100 mW cm^{-2}. SEM images displaying the surface morphology of PEDOT:PSS/P-TPD/QD/ZnO films after being subjected to (d) 0 folding cycle, (e) 50 folding cycles and (f) 150 folding cycles.

4. Conclusion

A QD-photodetector incorporating a double PEDOT:PSS/P-TPD HTL structure was fabricated *via* solution-processing methods onto a flexible substrate. By the addition of P-TPD to form a double HTL, the hole transport efficiency was significantly enhanced. Due to the high LUMO energy level of the P-TPD, electron transport to the HTL was effectively blocked. As a consequence, the photodetector exhibited a broad spectral response encompassing the ultraviolet-visible-near infrared (UV-NIR) region, a high specific detectivity of 2.6×10^{12} Jones, a fast response speed of 40 ms, and a high responsivity of 45 mA W^{-1} with extreme flexibility. The detectivity is higher that of the reported flexible QD-photodetectors, and is comparable to rigid devices with the same architecture. More importantly, an excellent photocurrent density (196×10^{-6} mA cm^{-2}) was observed for the double HTL-based photodetector under weak light illumination (5 μW cm^{-2}). The flexible device also showed excellent folding endurance and electrical stability after bending 150 cycles. Our results suggest that such high-performance flexible photodetectors may have great potential for monitoring, communications and imaging applications.

Conflicts of interest

There are no conflicts to declare.

Acknowledgements

Financial support from the National Science Foundation of China (51961135107, 51774034, 51772026), the National Key Research and Development Program of China (2017YFE0119700), and the Beijing Natural Science Foundation (2182039) is gratefully acknowledged.

References

1 X. Peng, *Nano Res.*, 2010, **2**, 425–447.
2 S. Ruhle, M. Shalom and A. Zaban, *ChemPhysChem*, 2010, **11**, 2290–2304.
3 W. W. Yu, L. QU, W. Guo and X. Peng, *Chem. Mater.*, 2003, **15**, 2854–2860.
4 G. H. Carey, A. L. Abdelhady, Z. Ning, S. M. Thon, O. M. Bakr and E. H. Sargent, *Chem. Rev.*, 2015, **115**, 12732–12763.
5 M. R. Kim and D. Ma, *J. Phys. Chem. Lett.*, 2015, **6**, 85–99.
6 J. Y. Kim, O. Voznyy, D. Zhitomirsky and E. H. Sargent, *Adv. Mater.*, 2013, **25**, 4986–5010.
7 E. H. Sargent, *Nat. Photonics*, 2012, **6**, 133–135.
8 T. Shen, J. J. Tian, L. L. Lv, C. B. Fei, Y. J. Wang, T. Pullerits and G. Z. Cao, *Electrochim. Acta*, 2016, **191**, 62–69.
9 J. Tian, L. Lv, C. Fei, Y. Wang, X. Liu and G. Cao, *J. Mater. Chem. A*, 2014, **2**, 19653–19659.
10 R. S. Sanchez, M. S. d. l. Fuente, I. Suarez, G. Muñoz-Matutano and J. P. Martinez-Pastor, *Science*, 2016, **2**, e1501104.
11 G. Walter, N. Holonyak, R. D. Heller and R. D. Dupuis, *Appl. Phys. Lett.*, 2002, **81**, 4604–4606.
12 V. Adinolfi, O. Ouellette, M. I. Saidaminov, G. Walters, A. L. Abdelhady, O. M. Bakr and E. H. Sargent, *Adv. Mater.*, 2016, **28**, 7264–7268.
13 D. Kufer, I. Nikitskiy, T. Lasanta, G. Navickaite, F. H. Koppens and G. Konstantatos, *Adv. Mater.*, 2015, **27**, 176–180.
14 Y. Wang, D. Yang, X. Zhou, D. Ma, A. Vadim, T. Ahamad and S. M. Alshehri, *Adv. Opt. Mater.*, 2017, **5**, 1700213.
15 C. Bao, J. Yang, S. Bai, W. Xu, Z. Yan, Q. Xu, J. Liu, W. Zhang and F. Gao, *Adv. Mater.*, 2018, **30**, e1803422.
16 R. E. Bailey and S. Nie, *J. Am. Chem. Soc.*, 2003, **125**, 7100–7106.
17 M. S. Park, V. Jain, W. J. Choi, H. Pettersson, Q. Wang, J. D. Song, E. H. Lee and S. H. Kim, *Electron. Lett.*, 2014, **50**, 1731–1733.
18 P. Martyniuk and A. Rogalski, *Bull. Pol. Acad. Sci.: Tech. Sci.*, 2009, **57**, 103.
19 P. Martyniuk and A. Rogalski, *Prog. Quantum Electron.*, 2008, **32**, 89–120.
20 L.-B. Luo, J.-J. Chen, M.-Z. Wang, H. Hu, C.-Y. Wu, Q. Li, L. Wang, J.-A. Huang and F.-X. Liang, *Adv. Funct. Mater.*, 2014, **24**, 2794–2800.
21 F. P. García de Arquer, A. Armin, P. Meredith and E. H. Sargent, *Nat. Rev. Mater.*, 2017, **2**, 16100.
22 M. Peng, Y. Wang, Q. Shen, X. Xie, H. Zheng, W. Ma, Z. Wen and X. Sun, *Sci. China Mater.*, 2019, **62**, 225–235.
23 V. Q. Dang, G.-S. Han, T. Q. Trung, L. T. Duy, Y.-U. Jin, B. U. Hwang, H.-S. Jung and N.-E. Lee, *Carbon*, 2016, **105**, 353–361.
24 S. Mitra, A. Aravindh, G. Das, Y. Pak, I. Ajia, K. Loganathan, E. Di Fabrizio and I. S. Roqan, *Nano Energy*, 2018, **48**, 551–559.
25 W. S. Lee, S. W. Lee, H. Joh, M. Seong, H. Kim, M. S. Kang, K. H. Cho, Y. M. Sung and S. J. Oh, *Small*, 2017, 1702534.
26 I. Ka, L. F. Gerlein, L. M. Asuo, R. Nechache and S. G. Cloutier, *Nanoscale*, 2018, **10**, 9044–9052.
27 X. Gong, M. Tong, Y. Xia, W. Cai, J. Moon, Y. Cao, G. Yu, C.-L. Shieh, B. Nilsson and A. J. Heeger, *Science*, 2009, **325**, 1665–1668.
28 X. Yi, Z. Ren, N. Chen, C. Li, X. Zhong, S. Yang and J. Wang, *Adv. Electron. Mater.*, 2017, **3**, 1700251.
29 S. Wang, C. Bi, J. Yuan, L. Zhang and J. Tian, *ACS Energy Lett.*, 2018, **3**, 245–251.
30 X. Z. Dai, Z. Jin, Y. Niu, Y. Cao, H. Liang, X. Chen, L. Wang and X. Peng, *Nature*, 2014, **515**, 96–110.
31 S. Pradhan, A. Stavrinadis, S. Gupta, S. Christodoulou and G. Konstantatos, *ACS Energy Lett.*, 2017, **2**, 1444–1449.
32 T. Shen, B. Li, K. Zheng, T. Pullerits, G. Cao and J. Tian, *J. Phys. Chem. Lett.*, 2018, **9**, 3285–3294.
33 Z. Ren, J. Sun, H. Li, P. Mao, Y. Wei, X. Zhong, J. Hu, S. Yang and J. Wang, *Adv. Mater.*, 2017, **29**, 1702055.
34 Y. Li, Y. Li, J. Shi, H. Zhang, J. Wu, D. Li, Y. Luo, H. Wu and Q. Meng, *Adv. Funct. Mater.*, 2018, 1705220.
35 H. Bai, T. Shen and J. Tian, *J. Mater. Chem. C*, 2017, **5**, 10543–10548.
36 G. Maculan, A. D. Sheikh, A. L. Abdelhady, M. I. Saidaminov, M. A. Haque, B. Murali, E. Alarousu, O. F. Mohammed, T. Wu and O. M. Bakr, *J. Phys. Chem. Lett.*, 2015, **6**, 3781–3786.
37 D. C. Oertel, M. G. Bawendi, A. C. Arango and V. Bulović, *Appl. Phys. Lett.*, 2005, **87**, 213505.
38 R. Guo, T. Shen and J. Tian, *J. Mater. Chem. C*, 2018, **6**, 2573–2579.
39 Z. Zheng, F. Zhuge, Y. Wang, J. Zhang, L. Gan, X. Zhou, H. Li and T. Zhai, *Adv. Funct. Mater.*, 2017, **27**, 1703115.
40 K. S. Cho, K. Heo, C. W. Baik, J. Y. Choi, H. Jeong, S. Hwang and S. Y. Lee, *Nat. Commun.*, 2017, **8**, 840.
41 F. Guo, B. Yang, Y. Yuan, Z. Xiao, Q. Dong, Y. Bi and J. Huang, *Nat. Nanotechnol.*, 2012, **7**, 798–802.
42 S. F. Leung, K. T. Ho, P. K. Kung, V. K. S. Hsiao, H. N. Alshareef, Z. L. Wang and J. H. He, *Adv. Mater.*, 2018, **27**, 1704611.
43 Z. Gao, W. Jin, Y. Zhou, Y. Dai, B. Yu, C. Liu, W. Xu, Y. Li, H. Peng, Z. Liu and L. Dai, *Nanoscale*, 2013, **5**, 5576–5581.
44 Y. Wei, Z. Ren, A. Zhang, P. Mao, H. Li, X. Zhong, W. Li, S. Yang and J. Wang, *Adv. Funct. Mater.*, 2018, **28**, 1706690.
45 J. Li, Z. Liang, Q. Su, H. Jin, K. Wang, G. Xu and X. Xu, *ACS Appl. Mater. Interfaces*, 2018, **10**, 3865–3873.
46 C. Fei, L. Guo, B. Li, R. Zhang, H. Fu, J. Tian and G. Cao, *Nano Energy*, 2017, **27**, 17–26.
47 M. Li, B. Li, G. Cao and J. Tian, *J. Mater. Chem. A*, 2017, **5**, 21313–21319.
48 T. Shen, B. Li, J. Tian and G. Cao, *Sci. China Mater.*, 2016, **59**, 833–841.
49 J. Tian, E. Uchaker, Q. Zhang and G. Cao, *ACS Appl. Mater. Interfaces*, 2014, **6**, 4466–4472.
50 A. Castan, H. M. Kim and J. Jang, *ACS Appl. Mater. Interfaces*, 2014, **6**, 2508–2515.
51 M.-H. Lee, L. Chen, N. Li and F. Zhu, *J. Mater. Chem. C*, 2017, **5**, 10555–10561.

